IOP Publishing Smart Materials and Structures
Smart Mater. Struct. **23** (2014) 125032 (13pp) doi:10.1088/0964-1726/23/12/125032

Contactless ultrasonic energy transfer for wireless systems: acoustic-piezoelectric structure interaction modeling and performance enhancement

S Shahab and A Erturk

G. W. Woodruff School of Mechanical Engineering, Georgia Institute of Technology, Atlanta, GA 30332, USA

E-mail: alper.erturk@me.gatech.edu

Received 29 May 2014, revised 11 July 2014
Accepted for publication 3 September 2014
Published 4 November 2014

Abstract

There are several applications of wireless electronic components with little or no ambient energy available to harvest, yet wireless battery charging for such systems is still of great interest. Example applications range from biomedical implants to sensors located in hazardous environments. Energy transfer based on the propagation of acoustic waves at ultrasonic frequencies is a recently explored alternative that offers increased transmitter-receiver distance, reduced loss and the elimination of electromagnetic fields. As this research area receives growing attention, there is an increased need for fully coupled model development to quantify the energy transfer characteristics, with a focus on the transmitter, receiver, medium, geometric and material parameters. We present multiphysics modeling and case studies of the contactless ultrasonic energy transfer for wireless electronic components submerged in fluid. The source is a pulsating sphere, and the receiver is a piezoelectric bar operating in the 33-mode of piezoelectricity with a fundamental resonance frequency above the audible frequency range. The goal is to quantify the electrical power delivered to the load (connected to the receiver) in terms of the source strength. Both the analytical and finite element models have been developed for the resulting acoustic-piezoelectric structure interaction problem. Resistive and resistive–inductive electrical loading cases are presented, and optimality conditions are discussed. Broadband power transfer is achieved by optimal resistive-reactive load tuning for performance enhancement and frequency-wise robustness. Significant enhancement of the power output is reported due to the use of a hard piezoelectric receiver (PZT-8) instead of a soft counterpart (PZT-5H) as a result of reduced material damping. The analytical multiphysics modeling approach given in this work can be used to predict and optimize the coupled system dynamics with very good accuracy and dramatically improved computational efficiency compared to the use of commercial finite element packages.

Keywords: piezoelectricity, wireless, energy transfer, energy harvesting, ultrasound

(Some figures may appear in colour only in the online journal)

1. Introduction

The harvesting of ambient vibrations for powering wireless electronic components has been heavily researched over the last decade [1–5]. As long as sufficient vibrational energy is readily available in the neighborhood of small electronic devices, it is possible to achieve mechanical-to-electrical energy conversion by means of a proper transduction mechanism and thereby enable self-powered wireless electronic systems. An alternative scenario is the case in which a wireless electronic component has little or no vibrational energy available in its environment, yet the wireless charging

of its battery is still of great interest and is possible by means of contactless energy transfer (CET). Examples of this scenario range from biomedical implants (e.g. cardiac pacemakers) to sensors located beyond physical access or in hazardous environments (e.g. sensors in nuclear waste containers). As an alternative to relatively well-studied methods of CET, namely the inductive, far-field electromagnetic (or microwave), capacitive and optical coupling methods [6], research in the field of ultrasonic acoustic energy transfer (UAET) has recently gained momentum for energy transmission to wireless electronic components in various applications.

In particular, biomedical applications offer great potential for CET since battery charging for medical implants without surgery is tremendously valuable, and the vibration intensity available inside of the body (from the organs that exhibit motion or dynamic strain) is usually very low for energy harvesting. It is worth mentioning that although the acceleration levels of muscular organs, such as the heart, have appeared intriguing to some researchers for energy harvesting [7], unfortunately, what matters is the available power (or intensity) because tissue and muscle are dramatically more compliant than standard lab shakers. In other words, a kinematic measurement (e.g. acceleration, velocity or displacement) in the absence of the harvester provides insufficient information to simulate vibrational energy available from a compliant, low-impedance system when using an electrodynamic shaker in a lab environment. Using the example of the heartbeat, the main limitation, therefore, is the impedance mismatch to have the same heartbeat acceleration in the presence of a non-compliant harvester. If the original heart wall acceleration in the absence of the harvester is a_o, it is straightforward to show that [8] the acceleration available in the presence of the harvester is $a_f = a_o/(1+\alpha)$, where $\alpha = Z_{harvester}/Z_{heart\_wall}$ is the harvester to heart wall impedance ratio at the mounting location, suggesting that the kinematic input available to the harvester will substantially diminish in the coupled system (after the harvester is mounted), since $\alpha \gg 1$ for strongly coupled piezoceramic harvesters, as in the cm-scale device reported in [7]. This leaves compliant materials (such as dielectric elastomers [9, 10] or ionic polymers-metal composites [11, 12]) as the only option to avoid a mechanical impedance mismatch at the expense of dramatically reduced power density (of electronic/ionic polymers) as the main trade off. On the other hand, using a proper CET method, such as UAET, it is possible to transfer usable energy (which is more than sufficient for pacemakers) within a range of several centimeters to charge the battery of a medical implant without surgery.

In UAET, the ultrasonic waves transfer acoustic energy from a vibrating source (also called the transmitter) to a piezoelectric receiver, which then converts the vibrational energy into electricity and delivers it to an electrical load. Among the methods of CET [6, 13–15], the relatively less-studied UAET approach is an effective method for biomedical applications toward powering implanted devices [16–22] due to the number of advantages it offers, while the most heavily investigated approach for CET remains inductive coupling [23–28]. In the latter method (inductive coupling), the power transfer is realized by means of two inductive resonators. High efficiency is achieved only within distances of the same order of the size of the transmitter and receiver coils, as the inductive coupling reduces significantly with the increased distance (which requires increased reactive currents; therefore high conduction losses occur). In addition, inductive coupling experiences losses at high frequencies involved [6]. The less popular capacitive coupling method is limited to very short distances for voltage levels to be realistic since capacitance is inversely proportional to distance. The other two methods are far-field electromagnetic coupling [13] and optical coupling [29] for CET. Recent analytical and experimental studies in the fields of both ultrasonic and inductive CET show that UAET is more advantageous for power transfer at large distances and for small implants [6, 21, 30]. Moreover, UAET is well suited for biomedical applications in which exposure to electromagnetic fields is not allowed.

A brief summary of the limited (and mostly experimental) literature on UAET follows next (more details can be found in a recent review article [6]). The first biomedical application of UAET for charging implants appears to be in the early work by Cochran *et al* [16, 17]. They presented a system based on an internal piezoelectric plate attached to the bone fracture site in order to provide mechanical stability. The piezoelectric element was excited by external ultrasonic waves and generated an electrical current that was delivered to the electrodes in order to stimulate treating the fractures. Remarkably, this [16, 17] early approach was also used for energy harvesting from the mechanical strain in the implanted device due to the body's motion. Recently, Kawanabe *et al* [18] and Suzuki *et al* [19] demonstrated ultrasonic power and information transmission to implanted medical devices. They could achieve an energy transfer efficiency of 20% and a 9.5 kb s^{-1} bit rate for a power supply operating at 1 MHz frequency. Ozeri and Shmilovitz [20] investigated ultrasonic transcutaneous energy transfer as a method for powering implant devices. In this method, two ultrasonic piezoelectric transducers were used as the external transmitter to the body and as the receiver implanted inside of the body. The measurements of ultrasonic radiation and energy transfer were conducted thorough pig muscle tissue, and the results showed a 27% power transfer efficiency (70 mW of the power output at a 5 mm distance) for an excitation frequency of 673 kHz. After that, Ozeri *et al* [21] proposed an ultrasonic transcutaneous energy transfer system similar to [20] with the aim of minimizing the diffraction losses by using segmented electrodes in the driver transducer. More recently, Maleki *et al* [22] presented an implantable micro-oxygen generator powered ultrasonically at 2.15 MHz. The experimental results obtained by the proposed method showed less directionality and greater power transmission efficiencies for larger penetration depth and smaller receiver dimensions compared to inductive transmission. In 2013, Roes *et al* [6] reviewed the methods of CET in detail along with available technologies of

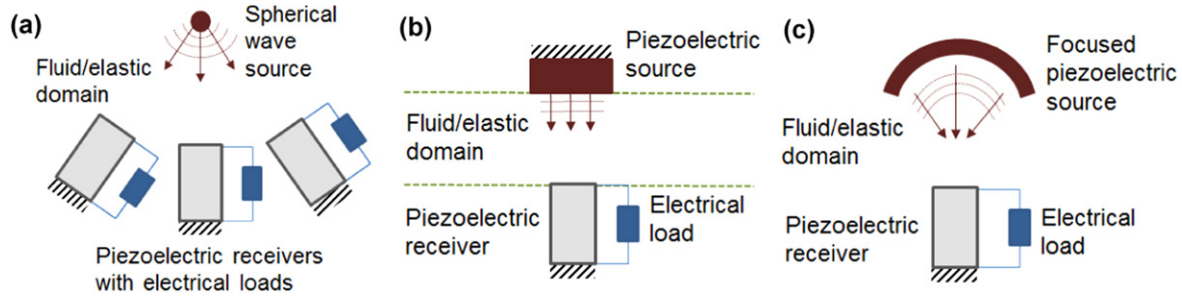

Figure 1. Example concepts of UAET using piezoelectric receiver bars (separately connected to electrical loads) operating in the 33-mode of piezoelectricity: (a) Excitation of an array of receivers by a pulsating sphere in the same domain; (b) excitation of a receiver by a disk/bar in separate domains (as in biomedical applications; the receiver is in the tissue domain); and (c) excitation by a focused transducer for spatial localization of the transmitted energy for enhanced excitation of the receiver.

UAET. Specifically, they [6] pointed out the lack of modeling efforts for UAET, which is the central theme of our present work, along with performance enhancement, as outlined in the next section.

2. UAET concepts and outline

The schematic representations of various possible and potential concepts in UAET are demonstrated in figure 1. The first one shown in figure 1(a) represents the energy transfer from a pulsating sphere to an array of piezoelectric receiver bars (which are separately shunted to electrical loads). Acoustic waves can be transmitted in various media, such as water, air or tissue, as long as the vibrating source is well coupled to the medium, i.e. the impedance mismatch between the source and the medium is minimized. For instance, in the absence of ambient energy to harvest, underwater sensor networks or other arrays of wireless electronic components can be powered by UAET, as depicted in figure 1(a). The second schematic (figure 1(b)) is analogous to the transcutaneous UAET concept studied by Ozeri *et al* [20, 21] for transferring energy from an external piezoelectric source to a piezoelectric receiver inside of the tissue (i.e. multiple domains are involved). Figure 1(b) may represent various other problems of more than one domain (medium). For instance, a third domain is often introduced to minimize a possible impedance mismatch between two domains of primary interest (e.g. the domains of the transmitter and receiver in UAET). The last schematic in figure 1(c) is implemented from the HIFU (high-intensity focused ultrasound) technology [31] to focus the transmitted energy in space and thereby strongly excite the receiver with dramatically reduced energy input to the source. This focusing should obviously be employed in UAET with care since HIFU may yield substantial energy localization and heating, which is the basis of its use in hyperthermia therapy [31] to destroy diseased or damaged tissue. It is worth mentioning that other than using curved piezoelectric transducers to create focusing, as depicted in figure 1(c), mirroring concepts [32] can also be employed with point sources in order to focus the transmitted energy in space.

In the present work, we explore the basic concept of figure 1(a), i.e. UAET from a pulsating spherical source to a receiver piezoelectric bar shunted to an electrical load. While the focusing concept (figure 1(c)) is suitable for exciting a single receiver, radiation from a spherical source (figure 1(a)) is a practical solution to power multiple wireless electronic components by using a single source. The application of the scenario in figure 1(a) is not limited to underwater sensor networks, and it could represent the powering of wireless electronic devices in another medium by means of a single source.

Although there has been growing interest in the field of UAET under the area of CET, fully coupled acoustic-piezoelectric structure interaction modeling that combines the source and the receiver dynamics with fluid coupling as well as the electrical load has not been covered in the existing literature. Analytical modeling and a closed-form solution of this electromechanical and acoustical problem can be used for the design and performance optimization of UAET concepts with substantially improved computational efficiency as compared to multiphysics finite element modeling. To this end, in the present paper, a coupled model is developed for the wireless acoustic energy transfer from a spherical wave source to the electrical load of a piezoelectric receiver (the special case of figure 1(a) with a single receiver). The fully coupled model relates the source strength to the electrical power output of the receiver through the acoustic-structure interaction at the receiver-fluid interface. The receiver is a thickness-poled piezoelectric transducer located at a specific distance from the source and is excited longitudinally by incident acoustic pressure waves. In the following, first, an *in vacuo* electromechanical model is developed for linear longitudinal vibration of a fixed-free cylindrical piezoelectric bar with the fundamental vibration mode. Then, in order to account for the acoustic-structure interaction, a lumped-parameter electromechanical piston representation of a fully submerged piezoelectric bar is used. The equivalent parameters are defined, and the *in vacuo* model is extended by adding the radiation impedance terms to the equation of motion. The effects of the various parameters, such as the source strength, source-to-receiver distance and receiver diameter, are explored. Both the resistive and resistive-reactive electrical loads are considered for the receiver bar. Soft

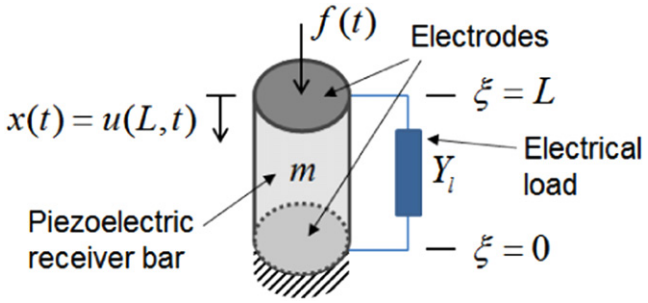

Figure 2. Longitudinal excitation of a fixed-free cylindrical piezoelectric receiver bar connected to an electrical load for power generation.

(PZT-5H) and hard (PZT-8) piezoelectric materials are considered for performance comparison.

3. Coupled modeling of UAET from a spherical wave source to a 33-mode receiver

3.1. In vacuo electromechanical dynamics of a 33-mode receiver

The linear constitutive equations for a thickness-poled (i.e. longitudinally poled) piezoelectric bar operating in 33-mode are [33–35]

$$S_3 = s_{33}^E T_3 + d_{33} E_3, \tag{1}$$

$$D_3 = d_{33} T_3 + \varepsilon_{33}^T E_3, \tag{2}$$

where S_3 is the strain, T_3 is the stress, D_3 is the electric displacement and E_3 is the electric field, while s_{33}^E is the elastic compliance at constant electric field; d_{33} is the piezoelectric strain constant, and ε_{33}^T is the permittivity component at constant stress. Based on equations (1) and (2), it is assumed that the excitation of the receiver is such that the elastic, coupling and dissipative nonlinearities [36–39] are not pronounced, i.e. linear piezoelectricity is assumed.

The coupled partial differential equation for the longitudinal vibrations of the receiver and the electrical circuit equation (figure 2) can be derived as

$$-YA\frac{\partial^2 u(\xi,t)}{\partial \xi^2} - c_\alpha \frac{\partial^3 u(\xi,t)}{\partial \xi^2 \partial t} + c_\beta \frac{\partial u(\xi,t)}{\partial t} + m\frac{\partial^2 u(\xi,t)}{\partial t^2} + \theta v(t)[\delta(\xi) - \delta(\xi - L)] = f(t)\delta(\xi - L), \tag{3}$$

$$C_p \frac{dv(t)}{dt} + Y_l v(t) + \int_0^L \theta \frac{\partial^2 u(\xi,t)}{\partial t \partial \xi} d\xi = 0, \tag{4}$$

where $u(\xi, t)$ is the displacement response of the bar at the axial position ξ and time t, Y is the Young's modulus at constant electric field, m is the mass per unit length, c_α is the stiffness-proportional damping coefficient, c_β is the mass-proportional damping coefficient[1], A is the cross-sectional area, θ is the electromechanical coupling term in the physical coordinates and $f(t) = Fe^{j\omega t}$ is the external harmonic force resultant at the free-end surface of the bar (where F is the force amplitude, ω is the frequency and j is the unit imaginary number). Furthermore, C_p and Y_l are the internal capacitance of the piezoelectric receiver and the admittance of the external load, respectively; $v(t)$ is the voltage output across the electrical load, and $\delta(\xi)$ is the Dirac delta function. As depicted in figure 2, the mechanical strain axis and the electrical poling axis (perpendicular to the surface electrodes) are coincidental; therefore, the receiver bar is employed in the 33-mode of piezoelectricity. The dielectric loss is neglected, although it can easily be included by using a complex permittivity that includes the loss tangent of the piezoelectric material. Two types of electrical loading are to be considered in this work: purely resistive (yielding $Y_l = 1/R_l$, where R_l is the load resistance) and resistive-reactive (yielding, under harmonic excitation at frequency ω, $Y_l(\omega) = 1/R_l + 1/j\omega L_l$ for resistive–inductive loading, and $Y_l(\omega) = 1/R_l + j\omega C_l$ for resistive–capacitive loading, where L_l is the load inductance connected to the load resistance in parallel and C_l is the load capacitance connected to the load resistance in parallel).

The linear displacement at the free end of the piezoelectric bar ($x(t)$ in figure 2, where $x(t) = u(L, t)$) due to the harmonic excitation at or around the fundamental longitudinal (axial) vibration mode, is obtained by modal analysis of the distributed-parameter electromechanical system with a focus on the first mode only (i.e. higher modes are excluded in the following). The longitudinal tip displacement of the bar at time t is then

$$x(t) = u(\xi, t)\,|_{\xi=L} = \phi(L)\eta(t), \tag{5}$$

where $\phi(L)$ and $\eta(t)$ are, respectively, the mass-normalized eigenfunction evaluated at $\xi = L$ (in figure 2) and the generalized modal coordinate of the longitudinal vibration mode for a fixed-free uniform bar. The mass normalized eigenfunction evaluated at the tip is obtained as $\phi(L) = \sqrt{2/\rho AL}\sin(\pi\xi/2L)\big|_{\xi=L} = \sqrt{2/\rho AL}$ (where ρ is the mass density of the piezoelectric bar), which satisfies the companion mass and stiffness forms of the orthogonally conditions (see, for instance, appendix C.2 in Erturk and Inman [34] for standard modal analysis derivations under short-circuit conditions).

The electromechanically coupled equations of the forced vibration and current balance are expressed for this lumped-parameter model (reduced from a distributed-parameter solution) as

$$\ddot{x}(t) + 2\zeta\omega_n \dot{x}(t) + \omega_n^2 x(t) - \phi^2(L)\theta v(t) = \phi^2(L) f(t), \tag{6}$$

$$C_p \dot{v}(t) + Y_l v(t) + \theta \dot{x}(t) = 0, \tag{7}$$

where $\omega_n = (\pi/2)\sqrt{1/s_{33}^E \rho L^2}$ is the fundamental short-circuit natural frequency, ζ is the viscous damping ratio (that is due to internal mechanical losses only in the *in vacuo* problem) and an overdot represents the differentiation with respect to time.

[1] Proportional damping is assumed to represent in-vacuo material dissipation (which can be merely due to the stiffness-proportional damping term c_α in the Kelvin–Voigt approximation).

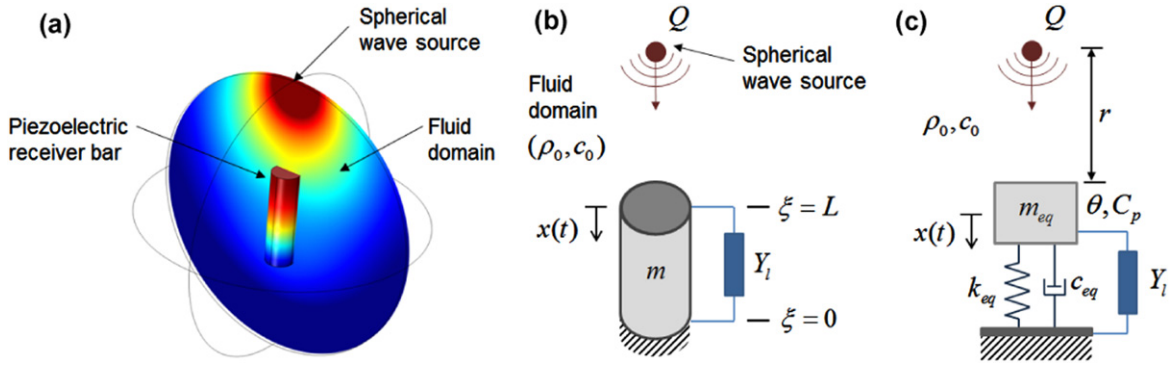

Figure 3. (a) Finite element simulation snapshot, (b) schematic representation and (c) lumped-parameter model of electrical power generation from spherical acoustic waves.

By substituting $x(t) = Xe^{j\omega t}$ and $v(t) = Ve^{j\omega t}$ for the steady state response, the single-mode tip displacement $x(t)$ and voltage response $v(t)$ of the longitudinal 33-mode configuration (figure 2) can be extracted from equations (6) and (7) as

$$x(t) = \frac{\left(Y_l(\omega) + j\omega C_p\right)F\phi^2(L)}{\left(\omega_n^2 - \omega^2 + j2\zeta\omega\omega_n\right)\left(Y_l(\omega) + j\omega C_p\right) + j\omega\theta^2\phi^2(L)}e^{j\omega t}, \quad (8)$$

$$v(t) = \frac{-j\omega\theta F\phi^2(L)}{\left(\omega_n^2 - \omega^2 + j2\zeta\omega\omega_n\right)\left(Y_l(\omega) + j\omega C_p\right) + j\omega\theta^2\phi^2(L)}e^{j\omega t}, \quad (9)$$

which are valid for vibrations with the fundamental longitudinal vibration mode, i.e. for excitations at or around the first longitudinal resonance frequency.

3.2. Acoustic-piezoelectric structure coupling and receiver power output

The fluid-loaded longitudinal vibration of the piezoelectric bar is based on a lumped-parameter electromechanical piston representation of the fully submerged piezoelectric receiver excited by incident acoustic pressure waves originating from a spherical source of known strength Q (figure 3). Therefore, the model development in this section is compatible with the lumped-parameter model reduced from the distributed-parameter formulation given in the previous section. We assume linear acoustics in the fluid (i.e. neither kinematic nor medium nonlinearities exist) and negligible loss in the fluid domain. Scatter pressure effects are also assumed to be negligible for the wavelength and receiver dimensions considered.

The electromechanically and acoustically coupled mechanical equation of motion for the lumped model in the x coordinate (figure 3(c)) can be written in the form of [34, 40]:

$$m_{eq}\ddot{x}(t) + c_{eq}\dot{x}(t) + k_{eq}x(t) + F_r(t) - \chi v(t) = f(t), \quad (10)$$

where m_{eq}, c_{eq}, k_{eq} and χ are the equivalent *in vacuo* mass, damping coefficient, stiffness and electromechanical coupling of the receiver, respectively. By multiplying both sides of equation (6) by m_{eq} and using the expression for short-circuit natural frequency ω_n, one can obtain the lumped-parameter terms as $m_{eq} = \rho AL/(\pi/2)^2$, $c_{eq} = 2m_{eq}\zeta\omega_n$, $k_{eq} = m_{eq}\omega_n^2$ and $\chi = m_{eq}\theta\phi^2(L)$. Furthermore, $f(t) = p(t)A$ is the resultant force due to the incident acoustic pressure wave evaluated at the piston's surface as$p(t) = Pe^{j\omega t}$ (where P is the complex pressure amplitude, and A is the piston area), and $F_r(t) = Z_r\dot{x}(t)$ is the force exerted by the fluid on the piston (where Z_r is the radiation impedance due to the acoustic-structure interaction at the free end of the receiver bar). The radiation impedance is given by $Z_r = R_r + jX_r$, where R_r and X_r are the resistive and reactive components for an unbaffled piston estimated using [35, 40]:

$$R_r = \sigma_R(ka)\rho_0 c_0 A\left(1 - \frac{J_1(2ka)}{ka}\right), \quad (11)$$

$$X_r = \sigma_X(ka)\rho_0 c_0 A\left(\frac{H_1(2ka)}{ka}\right). \quad (12)$$

Here, $J_1(2ka)$ and $H_1(2ka)$ are the first-order Bessel and Struve functions of the first kind, respectively [40], while $\sigma_R(ka)$ and $\sigma_X(ka)$ account for the modifications relative to the baffled problem (see, for instance, figure 10.19 in [35]). Moreover, $k = \omega/c_0$ is the wave number, c_0 is the speed of sound in fluid (e.g. water) surrounding the piston, ρ_0 is the mass density of the surrounding fluid and a is the radius of the piston (i.e. radius of the receiver's cross section: $a = \sqrt{A/\pi}$). The pressure field created by a pulsating spherical harmonic wave source in an infinite, homogeneous and isotropic medium is [40, 41]:

$$p(t) = \rho_0 c_0 \frac{-jkQ}{4\pi r\left(1 - jk\bar{a}\right)}e^{j\left(\omega t + k(r - \bar{a})\right)}, \quad (13)$$

where r is the source-to-receiver distance, and $\bar{a}$ is the source radius. Moreover, Q is the acoustic source strength, which is defined as a product of surface velocity U_0 and surface area $(4\pi\bar{a}^2)$ of the pulsating spherical wave source, i.e. $Q = 4\pi\bar{a}^2U_0$.

The single-mode tip displacement, voltage response and power output (normalized with respect to source strength)

frequency response functions for longitudinal vibrations of the fluid-loaded piezoelectric receiver are obtained using equations (10) and (7) as follows:

$$\left|\frac{x(t)}{Qe^{j(\omega t+k(r-\bar{a}))}}\right| = \left|\frac{-\rho_0 c_0 A\left(Y_l(\omega)+j\omega C_p\right)\times\left(\frac{jk}{4\pi r\left(1-jk\bar{a}\right)}\right)m_{eq}\phi^2(L)}{\left[-\left(m_{eq}+m_r\right)\omega^2+m_{eq}\omega_n^2+j\omega\left(2\xi m_{eq}\omega_n+R_r\right)\right]\times\left(Y_l(\omega)+j\omega C_p\right)+j\omega m_{eq}\theta^2\phi^2(L)}\right|, \tag{14}$$

$$\left|\frac{v(t)}{Qe^{j(\omega t+k(r-\bar{a}))}}\right| = \left|\frac{\rho_0 c_0 A j\omega\theta\left(\frac{jk}{4\pi r\left(1-jk\bar{a}\right)}\right)\times m_{eq}\phi^2(L)}{\left[-\left(m_{eq}+m_r\right)\omega^2+m_{eq}\omega_n^2+j\omega\left(2\xi m_{eq}\omega_n+R_r\right)\right]\times\left(Y_l(\omega)+j\omega C_p\right)+j\omega m_{eq}\theta^2\phi^2(L)}\right|, \tag{15}$$

$$\left|\frac{\Pi(t)}{\left(Qe^{j(\omega t+k(r-\bar{a}))}\right)^2}\right| = \frac{1}{R_l}\left|\frac{\rho_0 c_0 A j\omega\theta\left(\frac{jk}{4\pi r\left(1-jk\bar{a}\right)}\right)\times m_{eq}\phi^2(L)}{\left[-\left(m_{eq}+m_r\right)\omega^2+m_{eq}\omega_n^2+j\omega\left(2\xi m_{eq}\omega_n+R_r\right)\right]\times\left(Y_l(\omega)+j\omega C_p\right)+j\omega m_{eq}\theta^2\phi^2(L)}\right|^2, \tag{16}$$

where $m_r = X_r/\omega$ is the radiation mass, i.e. added mass, due to the reactive term given by equation (12), and Π stands for the electrical power output (to avoid confusion with the pressure amplitude P). In the above formulation, the dielectric loss can easily be added by changing the real-valued capacitance C_p to the complex form of $C_p(1-j\tan\delta)$, where $\tan\delta$ is the loss tangent of the piezoelectric material.

4. Optimal power and performance enhancement by resistive-reactive loading

4.1. Purely resistive electrical loading

The electrical load admittance in the presence of a purely resistive load of R_l is simply $Y_l = 1/R_l$. Then, the expression for the power output normalized with respect to the incident acoustic pressure amplitude on the surface is obtained from equation (16) as:

$$\left|\frac{\Pi}{P^2}\right| = \frac{\omega_{n,fluid}}{k_{eq}}\frac{\alpha A^2\kappa^2\tilde{\omega}^2}{\left[\left(1-\tilde{\omega}^2\right)-2\zeta_t\alpha\tilde{\omega}^2\right]^2+\left[\left(1+\kappa^2-\tilde{\omega}^2\right)\times\alpha\tilde{\omega}+2\zeta_t\tilde{\omega}\right]^2}, \tag{17}$$

where $\omega_{n,fluid}$ is the natural frequency of the receiver bar submerged in fluid, and the remaining parameters are dimensionless load resistance α, dimensionless system electromechanical coupling term κ^2, dimensionless excitation frequency $\tilde{\omega}$ and total damping ratio (in fluid) ζ_t:

$$\alpha = R_l C_p \omega_{n,fluid},\quad \kappa^2 = \frac{\theta^2}{k_{eq}C_p},\quad \tilde{\omega} = \frac{\omega}{\omega_{n,fluid}},\quad \zeta_t = \zeta_s + \frac{R_r}{2\left(m_{eq}+m_r\right)\omega_{n,fluid}}. \tag{18}$$

The optimal electrical load [42] that gives the maximum power output can then be obtained as:

$$\alpha_{opt}^2 = \left(R_{l,opt}C_p\omega_{n,fluid}\right)^2 = \frac{1}{\tilde{\omega}^2}\frac{\left(1-\tilde{\omega}^2\right)+\left(2\zeta_t\tilde{\omega}\right)^2}{\left(1+\kappa^2-\tilde{\omega}^2\right)^2+\left(2\zeta_t\tilde{\omega}\right)^2}, \tag{19}$$

which can be substituted into equation (17) to yield:

$$\left|\frac{\Pi_{opt}}{P^2}\right| = \frac{\omega_{n,fluid}}{k_{eq}}\frac{\alpha_{opt}A^2\kappa^2\tilde{\omega}^2}{\left[\left(1-\tilde{\omega}^2\right)-2\zeta_t\alpha_{opt}\tilde{\omega}^2\right]^2+\left[\left(1+\kappa^2-\tilde{\omega}^2\right)\times\alpha_{opt}\tilde{\omega}+2\zeta_t\tilde{\omega}\right]^2}. \tag{20}$$

4.2. Resistive–inductive electrical loading

For the case of resistive–inductive loading (the resistive load, R_l, and the inductive load, L_l, are connected in parallel),

$Y_l(\omega) = 1/R_l + 1/j\omega L_l$, and the power output normalized with respect to the incident pressure amplitude on the surface is:

$$\left|\frac{\Pi}{P^2}\right| = \frac{k_{eq}\alpha\beta^2 A^2\kappa^2\tilde{\omega}^4/\left(m_{eq}+m_r\right)^2}{\omega_{n,\,fluid}^3\left\{\left[\left(\beta+2\alpha\zeta_t\right)\tilde{\omega}-\beta\left(1+2\alpha\zeta_t\right)\tilde{\omega}^3\right]^2 + \left[\alpha-\left(2\beta\zeta_t+\alpha\left(1+\beta+\beta\kappa^2\right)\right)\tilde{\omega}^2 + \alpha\beta\tilde{\omega}^4\right]^2\right\}}, \quad (21)$$

where

$$\alpha = R_l C_p \omega_{n,fluid}, \quad \beta = L_l C_p \omega_{n,\,fluid}^2, \quad (22)$$

Following an optimization process in the same vein as Renno *et al* [43], the optimal resistive and inductive loads are obtained as:

$$\alpha_{opt} = R_{l,opt}\omega_{n,fluid}C_p = \frac{\tilde{\omega}^4+\left(4\zeta_t{}^2-2\right)\tilde{\omega}^2+1}{2\zeta_t\kappa^2\tilde{\omega}^2}, \quad (23)$$

$$\beta_{opt} = L_{l,opt}\omega_{n,\,fluid}^2 C_p = \frac{\tilde{\omega}^4+\left(4\zeta_t{}^2-2\right)\tilde{\omega}^2+1}{\tilde{\omega}^2\left(\tilde{\omega}^4-\left(2+\kappa^2-4\zeta_t{}^2\right)\tilde{\omega}^2+\kappa^2+1\right)}, \ \tilde{\omega}<\tilde{\omega}_{sc} \text{ and } \tilde{\omega}>\tilde{\omega}_{oc} \quad (24)$$

Substituting equations (23) and (24) into equation (21) yields:

$$\left|\frac{\Pi_{opt}}{P^2}\right| = \frac{k_{eq}A^2}{8\zeta_t\omega_{n,\,fluid}^3\left(m_{eq}+m_r\right)^2}, \ \tilde{\omega}<\tilde{\omega}_{sc} \text{ and } \tilde{\omega}>\tilde{\omega}_{oc} \quad \text{(for resistive-inductive loading)} \quad (25)$$

It should be noted that β_{opt} given by equation (24) is valid only outside the short- and open-circuit resonance frequencies [43], i.e. for $\tilde{\omega}<\tilde{\omega}_{sc}$ and $\tilde{\omega}>\tilde{\omega}_{oc}$, therefore equation (25) is valid only for this range under optimal resistive–inductive loading. The optimal inductance given by equation (24) would be negative between the short- and open-circuit resonance frequencies, implying that optimal capacitive tuning should be performed for $\tilde{\omega}_{sc}<\tilde{\omega}<\tilde{\omega}_{oc}$, as discussed next.

4.3. Resistive–capacitive electrical loading

For the case of resistive–capacitive loading (the resistive load, R_l, and the capacitive load, C_l, are connected in parallel), $Y_l(\omega) = 1/R_l + j\omega C_l$, and the power output normalized with respect to the incident pressure amplitude on the surface is

$$\left|\frac{\Pi}{P^2}\right| = \frac{k_{eq}\alpha A^2\kappa^2\tilde{\omega}^4/\left(m_{eq}+m_r\right)^2}{\omega_{n,\,fluid}^3\left\{\left[\left(2\alpha\gamma\zeta_t\tilde{\omega}^2-1\right)\tilde{\omega}+\left(1+2\alpha\zeta_t\right)\tilde{\omega}^3\right]^2 + \left[\alpha\gamma\left(1-\tilde{\omega}^2\right)+2\zeta_t + \alpha\left(1+\kappa^2-\tilde{\omega}^2\right)\right]^2\tilde{\omega}^4\right\}}, \quad (26)$$

where

$$\alpha = R_l C_p \omega_{n,fluid}, \quad \gamma = C_l/C_p \quad (27)$$

yielding the following optimal parameters:

$$\alpha_{opt} = R_{l,opt}\omega_{n,fluid}C_p = \frac{\tilde{\omega}^4+\left(4\zeta_t{}^2-2\right)\tilde{\omega}^2+1}{2\zeta_t\kappa^2\tilde{\omega}^2}, \quad (28)$$

$$\gamma_{opt} = C_{l,opt}/C_p = \frac{-\left(\tilde{\omega}^4-\left(2+\kappa^2-4\zeta_t{}^2\right)\tilde{\omega}^2+\kappa^2+1\right)}{\tilde{\omega}^4+\left(4\zeta_t{}^2-2\right)\tilde{\omega}^2+1}, \quad \tilde{\omega}_{sc}<\tilde{\omega}<\tilde{\omega}_{oc}. \quad (29)$$

Using equations (28) and (29) in equation (26) leads to

$$\left|\frac{\Pi_{opt}}{P^2}\right| = \frac{k_{eq}A^2}{8\zeta_t\omega_{n,\,fluid}^3\left(m_{eq}+m_r\right)^2}, \ \tilde{\omega}_{sc}<\tilde{\omega}<\tilde{\omega}_{oc} \quad \text{(for resistive–capacitive loading)}, \quad (30)$$

which is identical to equation (25) but valid for frequencies between the short- and open-circuit resonance values, i.e. for $\tilde{\omega}_{sc}<\tilde{\omega}<\tilde{\omega}_{oc}$, in capacitance tuning.

Briefly, the optimal resistive–inductive loading results in broadband power output for $\tilde{\omega}<\tilde{\omega}_{sc}$ and $\tilde{\omega}>\tilde{\omega}_{oc}$, while the optimal resistive–capacitive loading yields broadband power output for $\tilde{\omega}_{sc}<\tilde{\omega}<\tilde{\omega}_{oc}$. Note that the resulting broadband power output (Π_{opt}/P^2) will not have a flat spectrum due to frequency-dependent fluid loading effects.

5. Case studies, model validation and performance enhancement

5.1. Receiver properties and finite element model simulations

Analytical model results are compared with numerical simulations performed by 3D finite element modeling (FEM) in COMSOL Multiphysics version 4.2 for model validation using fixed-free boundary conditions. The receiver investigated in this case study is a cylindrical PZT-5H bar submerged in water (with thickness $L = 20$ mm and diameter $d = 6$ mm). The material properties are listed in table 1. Among the standard parameters of PZT-5H, the mechanical quality factor is assumed to be the only source of *in vacuo* dissipation; this is a reasonable assumption (since external fluid damping is already incorporated by the model). Therefore, the purely mechanical (material) damping ratio is approximated as 0.77% based on the mechanical quality

Table 1. Material properties of the PZT-5H receiver bar used in analytical and FEM simulations ($\varepsilon_0 = 8.854$ pF m^{-1} is the permittivity of free space, and $Q_m = 65$ is the mechanical quality factor).

Material	PZT-5H
Elastic compliance, $s_{33}^E \left[\text{pm}^2\ \text{N}^{-1}\right]$	20.7
Mass density, $\rho \left[\text{kg m}^{-3}\right]$	7500
Piezoelectric constant, $d_{33} \left[\text{pm V}^{-1}\right]$	593
Relative permittivity, $\varepsilon_{33}^T/\varepsilon_0$	3400
Equivalent capacitance, $C_p = \varepsilon_{33}^T A/\text{L}$ [pF]	42.5
Electromechanical coupling, $\theta \left[\text{C m}^{-1}\right]$	0.067
Mechanical damping ratio, $\zeta = 1/2Q_m$	0.0077

factor of PZT-5H in this table. The dielectric loss is neglected, although it can easily be included.

Figure 4 shows a typical demonstration of spherical wave excitation for a fixed-free fully submerged piezoelectric receiver bar over one period of excitation at its fundamental resonance frequency under open-circuit condition (47.7 kHz). The details of the spherical source location and the piezoelectric bar were previously shown in figure 3(a). The acoustic pressure field in the fluid domain and the piezoelectric longitudinal displacements are shown in each subgraph.

In the following sections, the goal is first to validate the analytical model with comparisons against finite-element simulations for different parameter values under open-circuit conditions. Then, the analytical model is employed to extract and optimize the transmitted power for finite values of load impedance under resistive and resistive-reactive electrical loading.

5.2. Analytical vs. finite element model frequency response results

The longitudinal displacement at the top end of the bar (x in the analytical derivation) and the voltage output are obtained from COMSOL as frequency response functions and compared with the analytical results. The relationships between the electromechanical outputs and system parameters, such as the distance of the receiver from the source (r), the level of source strength (Q) and the receiver diameter (d), are explored and shown in Figs. 5–7.

Figure 5 shows that the mechanical and electrical response amplitudes decrease monotonically as the source-to-receiver distance increases. The dependence of the response amplitude to the distance from the source is nonlinear (which makes sense from the analytical standpoint due to the hyperbolic dependence of the pressure to distance r in equation (13)). The results show very good agreement between the analytical and numerical (FEM) predictions.

Next, the variations of vibration (longitudinal tip displacement) and voltage frequency response magnitudes of the receiver with source strength are shown in figure 6. The results indicate that increasing source strength, amplifies the response of the receiver significantly. It is worth mentioning that the small-amplitude approximation [40] (the assumption used in equation (13)) requires that the displacement of the source surface should be much less than the radius of the source $\left(U_0/\omega \ll \bar{a}\right)$.

Figure 7 shows the effects of receiver diameter on the electromechanical frequency response functions. It is observed that with the increased cross-sectional area of the receiver, the underwater resonance frequency shifts to the left slightly; additionally, the peak vibration and voltage amplitudes decrease significantly. This is because the acoustic radiation resistance (or added damping) and reactance (or radiation added mass) are amplified in equations (11) and (12) due to the increased piston area (i.e. cross-sectional area) that vibrates against the fluid loading at the free end of the receiver bar. Therefore, in order to minimize, in particular, the radiation damping of the receiver bar, it may be preferable to reduce the cross-sectional area of the surface that interacts with the fluid. It should be noted that, while the voltage output decreases with increased receiver diameter, the capacitance increases, yielding increased current extraction.

5.3. Power output for resistive and resistive-reactive loading

Having validated the analytical model results for open-circuit conditions against 3D FEM simulations, finite load resistance cases are considered next (which cannot be easily simulated in a standard FEM environment). The purely resistive loading case is considered first ($Y_l = 1/R_l$ is the load admittance). Figure 8(a) shows the longitudinal tip displacement FRFs obtained from equation (14) for a set of resistors and for a broad range of frequencies, which cover the fundamental vibration mode, and for fixed values of distance from the source ($r = 20$ mm) and diameter of the piezoelectric receiver ($d = 6$ mm). The frequency response curves are given per source strength in agreement with equation (14). The electrical load resistance values range from 100 Ω (close to short-circuit conditions) to 100 MΩ (close to open-circuit conditions). As the load resistance is increased, the resonance frequency shifts from the short-circuit resonance frequency (31.4 kHz) to the open-circuit resonance frequency (47.7 kHz). From figure 8(a), one can observe that with the increased load resistance, the peak vibration amplitude decreases significantly from the peak of the short-circuit condition to a certain value, and then is amplified toward the open-circuit resonance frequency with a further increase in load resistance. This phenomenon happens because of the changing electrical boundary condition of the receiver (which alters the elastic modulus) and Joule heating (for moderate values of load resistance), as in standard vibration-based piezoelectric energy harvesters [34, 44]. In figure 8(b), by changing the electrical load resistance from short- to open-circuit conditions, the voltage output obtained from equation (15) increases monotonically at each frequency, and the resonance frequency of each finite load resistance takes a value between the short- and open-circuit resonance frequencies.

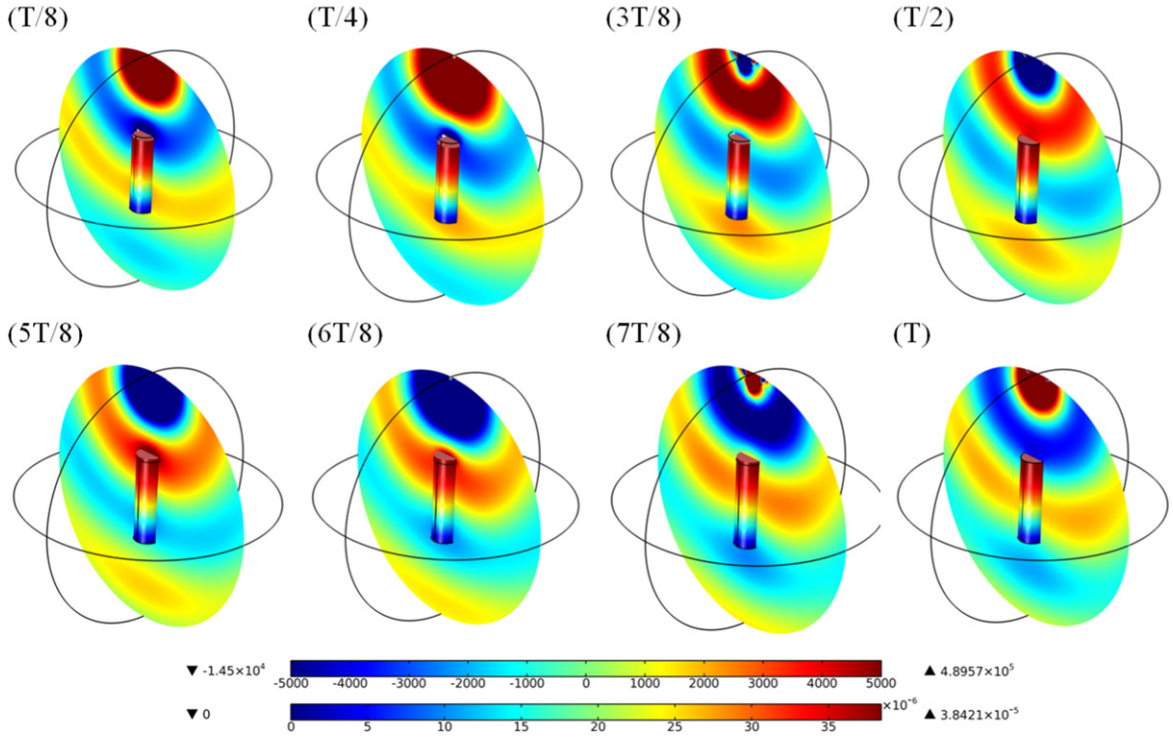

Figure 4. Multiphysics finite-element simulation for spherical wave excitation of a fixed-free piezoelectric receiver bar submerged under water under open-circuit condition. The acoustic pressure in the fluid domain (first color bar, in Pa) and the longitudinal displacement of the piezoelectric bar at its free end (second color bar, in mm) are shown for one period (T) of harmonic excitation at the fundamental open-circuit resonance frequency (47.7 kHz).

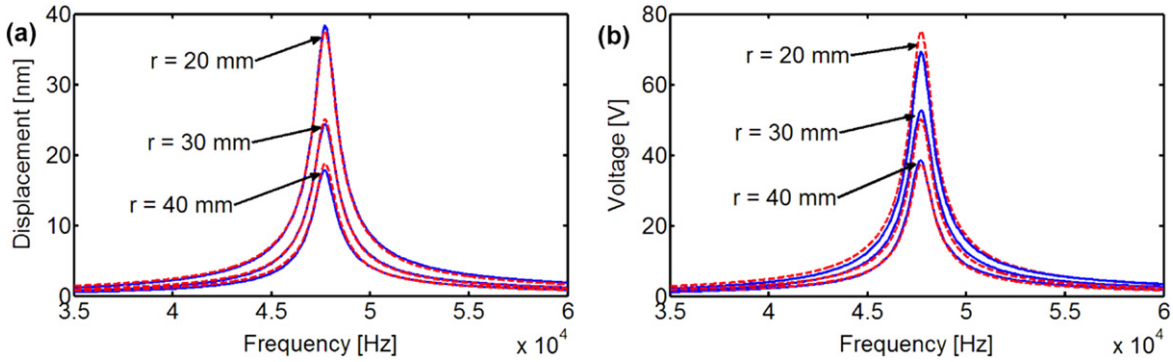

Figure 5. Comparison of the analytical (red dashed lines) and FEM (blue solid lines) frequency response curves for different values of source-to-receiver distance (r) under open-circuit conditions: (a) longitudinal tip displacement and (b) voltage output of the receiver bar ($Q = 5.65$ cm^3 s^{-1}; $d = 6$ mm).

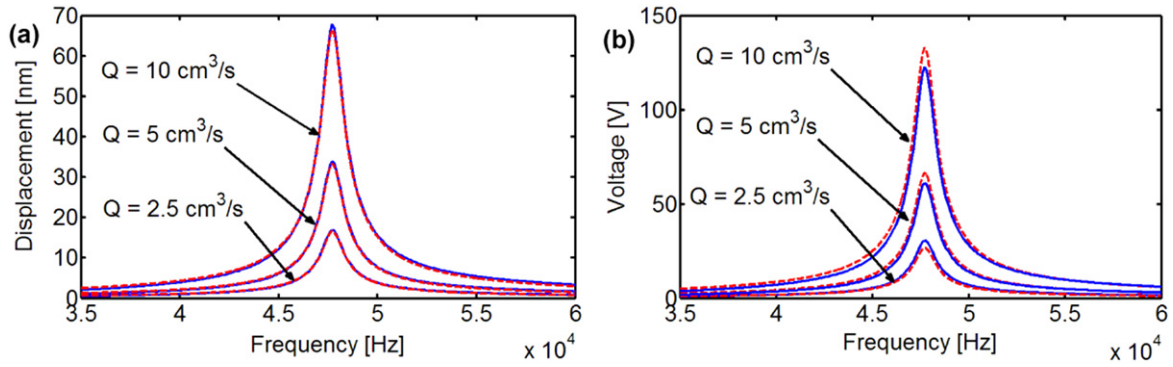

Figure 6. Comparison of the analytical (red dashed lines) and FEM (blue solid lines) frequency response curves for different values of source strength (Q) under open-circuit conditions: (a) longitudinal tip displacement and (b) voltage output of the receiver bar ($r = 20$ mm; $d = 6$ mm).

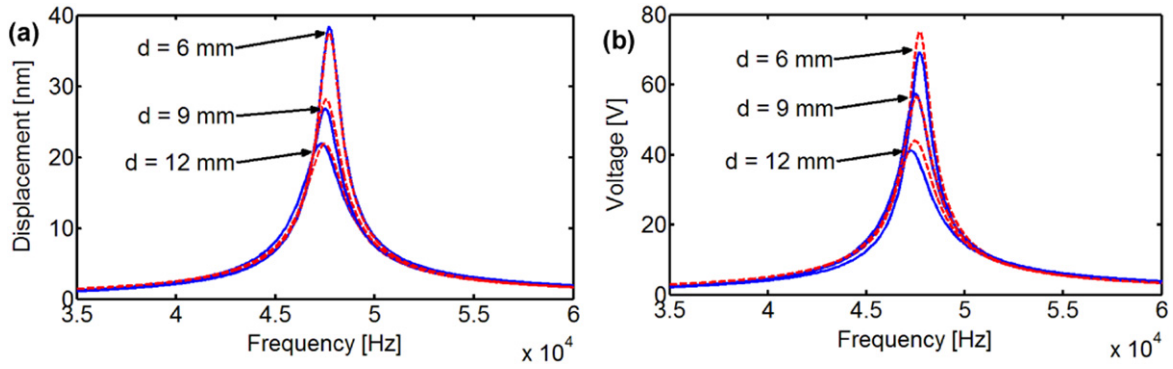

Figure 7. Comparison of the analytical (red dashed lines) and FEM (blue solid lines) frequency response curves for different values of receiver diameter (d) under open-circuit conditions: (a) longitudinal tip displacement and (b) voltage output of the receiver bar ($Q = 5.65\ \text{cm}^3\ \text{s}^{-1}$, $r = 20$ mm).

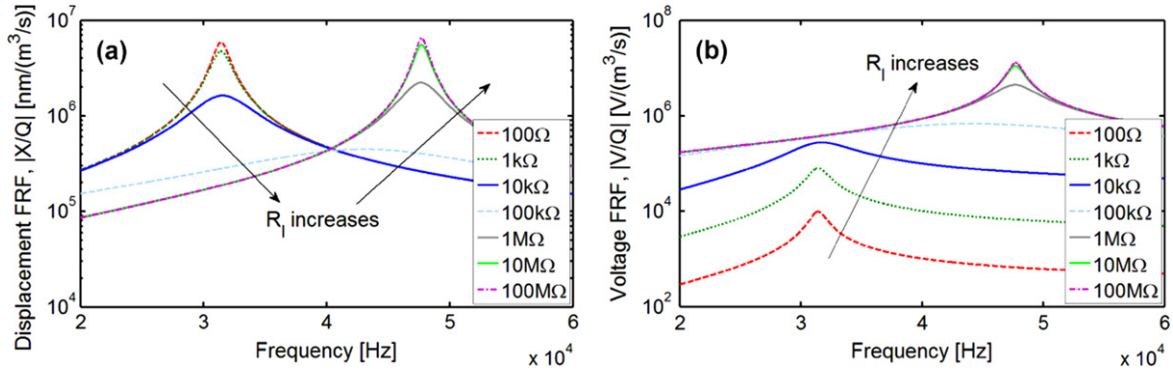

Figure 8. (a) Tip displacement-to-source strength FRFs and (b) voltage output-to-source strength FRFs of the receiver for a broad range of load resistance ($r = 20$ mm, $d = 6$ mm).

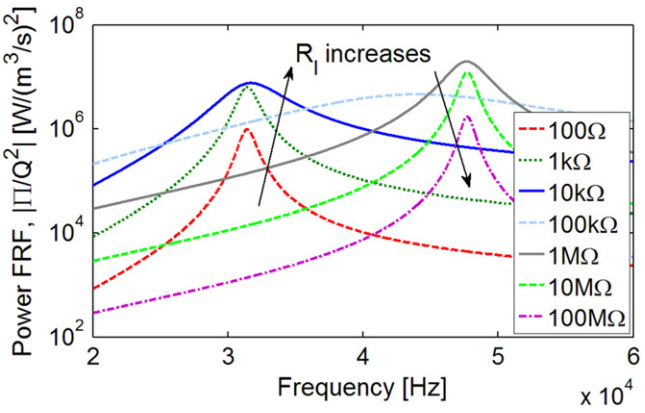

Figure 9. Power output-to-source strength FRFs of the receiver for a set of electrical load resistance values ($r = 20$ mm, $d = 6$ mm).

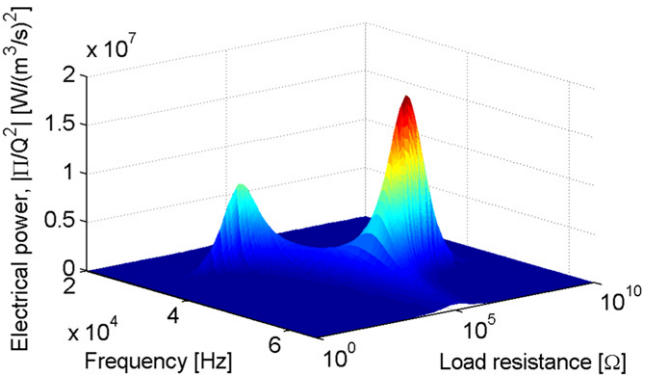

Figure 10. Power output (normalized with respect to the source strength squared) for the PZT-5H receiver versus the excitation frequency and load resistance ($r = 20$ mm, $d = 6$ mm).

The electrical power FRFs obtained from equation (16) are plotted in figure 9 for the same set of resistors. An optimal resistive load can be found at each excitation frequency. Among the finite set of resistance values in this graph, the maximum power output is obtained for the load resistance of 1 MΩ close to the open-circuit resonance frequency. However, the optimal electrical load changes dramatically with the changing excitation frequency. A more global picture is explored next using equation (16) to construct a surface plot.

The power output of the receiver bar normalized with respect to the source strength squared versus the load resistance and excitation frequency is plotted in figure 10 for fixed values of distance from the source ($r = 20$ mm) and diameter of the piezoelectric receiver ($d = 6$ mm). The resonance frequency smoothly shifts from the short-circuit value (31.4 kHz) to the open-circuit value (47.7 kHz). The local peak power at 31.4 kHz is 8.82 μW/(cm^3/s)^2 for the electrical load of 2.5 kΩ, while the global peak at 47.7 kHz is 18.8 μW/(cm^3/s)^2 for the optimal load of 2.5 MΩ. It is important to

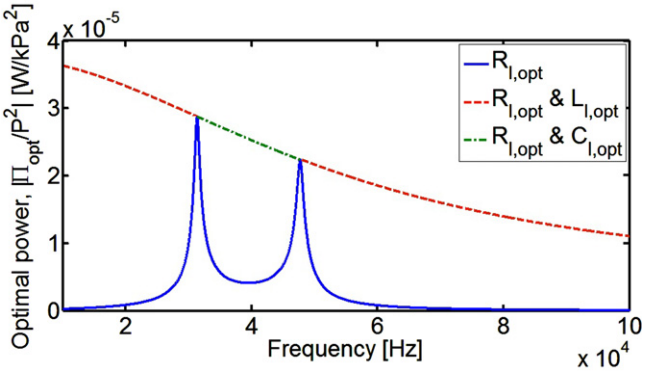

Figure 11. Optimal receiver power output frequency response curves (normalized by the incident acoustic pressure squared acting on the free end surface of the receiver) for the optimal resistive and resistive-reactive electrical loading cases.

note that the short- and open-circuit resonance excitations with the same source strength do not yield the same power output for the PZT-5H receiver, as a result of significant damping effects in fluid (soft piezoelectric receiver combined with fluid damping).

The resistive and resistive-reactive load optimization results (for power output normalized by the incident acoustic pressure squared acting on the free-end surface of the receiver) discussed in section 4 are plotted in figure 11 for the optimal purely resistive circuit, for the optimal resistive–inductive circuit (for frequencies less than 31.4 kHz and greater than 47.7 kHz), and for the optimal resistive–capacitive circuit (for frequencies in between 31.4 kHz and 47.7 kHz). It is clearly demonstrated that by optimizing the inductor/capacitor and resistor values simultaneously, broadband power generation is successfully achieved over a range of frequencies. The broadband power amplitude behavior is not flat (unlike the case of optimal resistive–inductive loading in vibration-based energy harvesters [43]) because of the fluid loading effects. It is worth adding that the inductance value required for conjugate matching is inversely proportional to the capacitance and frequency squared in equation (24). As long as the inductance requirement is low enough, a passive inductor can be employed for broadband behavior. To keep the inductance requirement low, a high-capacitance piezoelectric stack transducer [45] can be used instead of a monolithic receiver (so that the μF-level capacitance is achieved instead of the pF/nF-level capacitance) for which the above formulating still applies without a loss of generality using the effective values of d_{33}^{eff} and C_p for the entire cylindrical stack [45]. Alternatively, the excitation frequency can be kept high to reduce the inductance requirement. Otherwise, in the case of a large inductance requirement, a synthetic inductor (or synthetic impedance) circuit [46, 47] would be necessary (and part of the transmitted power would have to be used for that).

5.4. The effect of receiver material: Case study for PZT-8

As the last case study, we intended to explore the same problem (with a focus on purely resistive electrical loading) for an alternative piezoelectric material: PZT-8. The material properties for the PZT-8 receiver bar are listed in table 2. The dimensions of the receiver, source-to-receiver distance, fluid parameters, etc are all kept the same as in the previous case study for PZT-5H; only the material properties are changed. The mechanical quality factor of PZT-8 $\left(Q_m = 1000\right)$ is more than an order of magnitude larger than that of PZT-5H $\left(Q_m = 65\right)$, whereas the piezoelectric constant of PZT-8 ($d_{33} = 225$ pm V^{-1}) is lower compared to the PZT-5H ($d_{33} = 593$ pm V^{-1}). The capacitance and stiffness values also differ, resulting in the system coupling term (κ^2) values of 0.88 and 1.54 for PZT-8 and PZT-5H, respectively[2]. Therefore, PZT-8 offers reduced mechanical loss (which is favorable) at the expense of reduced electromechanical coupling compared to PZT-5H.

Table 2. Material properties of the PZT-8 receiver bar $\left(Q_m = 1000\right)$ used for performance comparison against the PZT-5H receiver.

Material	PZT-8
Elastic compliance, $s_{33}^E\left[\text{pm}^2\,\text{N}^{-1}\right]$	13.5
Mass density, $\rho\left[\text{kg m}^{-3}\right]$	7600
Piezoelectric constant, $d_{33}\left[\text{pm V}^{-1}\right]$	225
Relative permittivity, $\varepsilon_{33}^T/\varepsilon_0$	1000
Equivalent capacitance, $C_p = \varepsilon_{33}^T A/\text{L}$ [pF]	12.5
Electromechanical coupling, $\theta\left[\text{C m}^{-1}\right]$	0.034
Mechanical damping ratio, $\zeta = 1/2Q_m$	0.0005

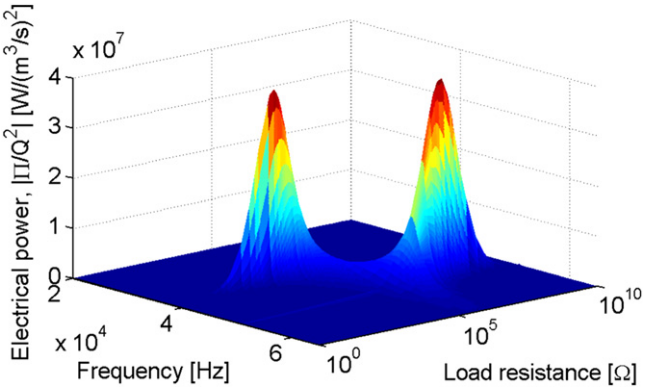

Figure 12. Power output (normalized with respect to the source strength squared) for the PZT-8 receiver versus the excitation frequency and load resistance ($r = 20$ mm, $d = 6$ mm).

The surface plot of the PZT-8 receiver's power output (normalized with respect to the source strength squared) versus the excitation frequency and load resistance is given in figure 12. As compared to the PZT-5H counterpart of this graph, previously given by figure 10, two things are noteworthy. First, the overall resonant power output of the PZT-8 receiver is larger than that of the PZT-5H receiver. Second, the short- and open-circuit resonance power outputs of the

[2] The receiver's system level coupling term (κ^2) should not be confused with the piezoelectric material's extensional coupling factor ($k_{33}^2 = d_{33}^2/s_{33}^E\varepsilon_{33}^T$), although they are related to each other.

PZT-8 receiver (which has lower mechanical damping, and therefore, lower total damping) are very similar to each other as in strongly coupled and lightly damped piezoelectric energy harvesters [34]. The short- and open-circuit resonance power output values are around 39 μW/(cm^3/s)^2 (for 3.5 kΩ and at 38.7 kHz) and 41 μW/(cm^3/s)^2 (for 15 MΩ and at 50.9 kHz), respectively. These resonant power outputs for the PZT-8 receiver are larger than those of the PZT-5H counterpart by factors of 4 and 2, respectively. Therefore, the hard ceramic PZT-8 (with reduced material loss at the expense of lower electromechanical coupling) should be preferred to the soft ceramic PZT-5H as the receiver material for resonant excitation. The same conclusion applies to soft versus hard single crystals [48, 49], e.g. PMN-PZT-Mn should be preferred to PMN-PT or PMN-PZT.

6. Conclusions

As an alternative to widely used methods of contactless energy transfer (such as inductive coupling), the use of piezoelectric transduction for the ultrasonic energy transfer to wireless electronic components (such as medical implants or sensors located in hazardous environments) has received growing attention over the last few years. However, fully coupled acoustic-piezoelectric structure interaction modeling that combines the source and the receiver dynamics with the fluid domain as well as the electrical load has not been covered in the existing literature. In this work, the contactless ultrasonic acoustic energy transfer is investigated by analytical and numerical multiphysics modeling along with several case studies with an emphasis on analytical model validation and performance enhancement. *In vacuo* and underwater dynamics of a cylindrical piezoelectric receiver are modeled for longitudinal vibrations under harmonic acoustic excitation. The fluid loading effects (resistive and reactive radiation impedance components) are added to the *in vacuo* electromechanical model to predict the underwater electromechanical response forms of the piezoelectric receiver. In addition to successful model validations against 3D finite element simulations, a study on the effects of several system parameters (e.g. source strength, receiver dimensions and source-to-receiver distance) is performed. Optimal resistive-reactive electrical loading results in a substantially enhanced broadband power transfer compared to the purely resistive electrical loading case. Soft (PZT-5H) and hard (PZT-8) piezoelectric receivers are considered, and significant performance enhancement is reported due to using PZT-8. Therefore, receivers made from hard piezoelectric ceramics (e.g. PZT-8, PZT-4) and single crystals (e.g. PMN-PZT-Mn) outperform those made from soft piezoelectric ceramics (e.g. PZT-5H, PZT-5A) and single crystals (e.g. PMN-PT, PMN-PZT) for resonant contactless power transfer. The electromechanically and acoustically coupled analytical model developed in this work can be used to predict and optimize the coupled system dynamics with very good accuracy and substantially improved computational efficiency compared to using commercial finite element simulation packages. Future work may explore energy focusing concepts [31, 32] and resulting acoustic nonlinearities [50] due to wave kinematics or medium, as well as transmitter/receiver electroelastic nonlinearities [36–39], and advanced electrical power conditioning circuits [51–57].

References

[1] Anton S R and Sodano H A 2007 A review of power harvesting using piezoelectric materials (2003–2006) *Smart Mater. Struct.* **16** R1

[2] Cook-Chennault K, Thambi N and Sastry A 2008 Powering MEMS portable devices—a review of non-regenerative and regenerative power supply systems with special emphasis on piezoelectric energy harvesting systems *Smart Mater. Struct.* **17** 043001

[3] Elvin N and Erturk A 2013 *Advances in Energy Harvesting Methods* (New York: Springer)

[4] Harne R and Wang K 2013 A review of the recent research on vibration energy harvesting via bistable systems *Smart Mater. Struct.* **22** 023001

[5] Daqaq M *et al* 2014 On the role of nonlinearities in vibratory energy harvesting: a critical review and discussion *Appl. Mech. Rev.* **66** 040801

[6] Roes M G L *et al* 2013 Acoustic energy transfer: a review *IEEE Trans. Indust. Electron.* **60** 242

[7] Amin Karami M and Inman D J 2012 Powering pacemakers from heartbeat vibrations using linear and nonlinear energy harvesters *Appl. Phys. Lett.* **100** 042901

[8] Fahy F J and Gardonio P 2007 *Sound and Structural Vibration: Radiation, Transmission and Response* (Oxford: Academic)

[9] Kornbluh R D *et al* 2011 From boots to buoys: promises and challenges of dielectric elastomer energy harvesting. in *Proc. SPIE* **7976** 797605

[10] McKay T G *et al* 2011 Soft generators using dielectric elastomers *Appl. Phys. Lett.* **98** 142903

[11] Dogruer D, Tiwari R and Kim K 2007 Ionic polymer metal composites as energy harvesters *The 14th Int Symp on: Smart Structures and Materials & Nondestructive Evaluation and Health Monitoring Int. Society for Optics and Photonics*

[12] Aureli M *et al* 2010 Energy harvesting from base excitation of ionic polymer metal composites in fluid environments *Smart Mater. Struct.* **19** 015003

[13] Brown W C 1984 The history of power transmission by radio waves *IEEE Trans. on Microwave Theory and Techniques* **32** 1230–42

[14] Brown W C 1996 The history of wireless power transmission *Solar Energy* **56** 3–21

[15] Dickinson R M 2003 Wireless power transmission technology state of the art the first Bill Brown lecture *Acta Astron* **53** 561–70

[16] Cochran G V *et al* 1985 Piezoelectric internal fixation devices: A new approach to electrical augmentation of osteogenesis *Journal of Orthopaedic Research* **3** 508–13

[17] Cochran G V, Kadaba M P and Palmieri V R 1988 External ultrasound can generate microampere direct currents *in vivo* from implanted piezoelectric materials *Journal of Orthopaedic Research* **6** 145–7

[18] Kawanabe H *et al* 2001 Power and information transmission to implanted medical device using ultrasonic *Japan. J. Appl. Phys.* **40** 3865

[19] Suzuki S-N *et al* 2002 Power and interactive information transmission to implanted medical device using ultrasonic *Japan. J. Appl. Phys.* **41** 3600–3
[20] Ozeri S and Shmilovitz D. 2010 Ultrasonic transcutaneousenergy transfer for powering implanted devices *Ultrasonics* **50** 556–66
[21] Ozeri S *et al* 2010 Ultrasonic transcutaneous energy transfer using a continuous wave 650 kHz Gaussian shaded transmitter *Ultrasonics* **50** 666–74
[22] Maleki T *et al* 2011 An ultrasonically powered implantable micro-oxygen generator (IMOG) *IEEE Trans. Biomed. Eng.* **58** 3104–11
[23] Olivo J, Carrara S and De Micheli G 2011 Energy harvesting and remote powering for implantable biosensors *IEEE Sensors Journal* **11** 1573–86
[24] Kurs A *et al* 2007 Wireless power transfer via strongly coupled magnetic resonances *Science* **317** 83–6
[25] Cannon B L *et al* 2009 Magnetic resonant coupling as a potential means for wireless power transfer to multiple small receivers *IEEE Trans. Power Electron.* **24** 1819–25
[26] Karalis A, Joannopoulos J D and Soljačić M 2008 Efficient wireless non-radiative mid-range energy transfer *Ann. of Appl. Phys.* **323** 34–48
[27] Sample A P, Meyer D A and Smith J R 2011 Analysis, experimental results, and range adaptation of magnetically coupled resonators for wireless power transfer *IEEE Trans. Indust. Electron* **58** 544–54
[28] Zhang F *et al* 2011 Relay effect of wireless power transfer using strongly coupled magnetic resonances *IEEE Trans. Magn.* **47** 1478–81
[29] Sahai A and Graham D 2011 Optical wireless power transmission at long wavelengths. in space optical systems and applications (ICSOS) *2011 IEEE Int. Conf. on*
[30] Denisov A and Yeatman E 2010 Ultrasonic vs. inductive power delivery for miniature biomedical implants. in body sensor networks (BSN) *2010 IEEE Int. Conf. on*
[31] ter Haar G and Coussios C 2007 High intensity focused ultrasound: physical principles and device *Int. J. Hyperthermia* **23** 89–104
[32] Carrara M *et al* 2012 Dramatic enhancement of structure-borne wave energy harvesting using an elliptical acoustic mirror *Appl. Phys. Lett.* **100** 204105
[33] Leo D J 2007 *Engineering Analysis of Smart Material Systems* (New Jersey: Wiley)
[34] Erturk A and Inman D J 2011 *Piezoelectric Energy Harvesting* (Chichester: Wiley)
[35] Sherman C H and Butler J L 2007 *Transducers and Arrays for Underwater Sound* (New York: Springer)
[36] Stanton S C *et al* 2010 Nonlinear piezoelectricity in electroelastic energy harvesters: modeling and experimental identification *J. Appl. Phys.* **108** 074903
[37] Stanton S C *et al* 2010 Resonant manifestation of intrinsic nonlinearity within electroelastic micropower generators *Appl. Phys. Lett.* **97** 254101
[38] Stanton S C *et al* 2012 Nonlinear nonconservative behavior and modeling of piezoelectric energy harvesters including proof mass effects *J. Intell. Material Systems and Structures* **23** 183–99
[39] Leadenham S and Erturk A 2014 Unified nonlinear electroelastic dynamics of a bimorph piezoelectric cantilever for energy harvesting, sensing, and actuation *Nonlinear Dynamics* (in press) doi:10.1007/s11071-014-1770-x
[40] Kinsler L E *et al* 1999 *Fundamentals of Acoustics* 1 (New York: Wiley)
[41] Pierce A D 1989 Acoustics: an introduction to its physical principles and applications *Acoustical Soc. of America*
[42] DuToit N E and Wardle B L 2007 Experimental verification of models for microfabricated piezoelectric vibration energy harvesters *AIAA journal* **45** 1126–37
[43] Renno J M, Daqaq M F and Inman D J 2009 On the optimal energy harvesting from a vibration source *J. Sound Vib.* **320** 386–405
[44] Lesieutre G A, Ottman G K and Hofmann H F 2004 Damping as a result of piezoelectric energy harvesting *J. Sound Vib.* **269** 991–1001
[45] Zhao S and Erturk A 2014 Deterministic and band-limited stochastic energy harvesting from uniaxial excitation of a multilayer piezoelectric stack *Sensors Actuators A: Physical* **214** 58–65
[46] Fleming A, Behrens S and Moheimani S 2000 Synthetic impedance for implementation of piezoelectric shunt-damping circuits *Electron. Lett.* **36** 1525–6
[47] Luo C, Whitehead M and Hofmann H 2009 Design and testing of a power electronic synthetic inductor *Int. J. Electron.* **96** 1249–64
[48] Cao H *et al* 2004 Elastic, piezoelectric, and dielectric properties of 0.58Pb (Mg 1/3 Nb 2/3) O 3-0.42PbTiO 3 single crystal *J. Appl. Phys.* **96** 549–54
[49] Zhang S *et al* 2008 Characterization of Mn-modified Pb (Mg 1/3 Nb 2/3) O 3–PbZrO 3–PbTiO 3 single crystals for high power broad bandwidth transducers *Appl. Phys. Lett.* **93** 122908
[50] Hamilton M F and Blackstock D T 1998 *Nonlinear acoustics* 237 (San Diego: Academic press)
[51] Ottman G K *et al* 2002 Adaptive piezoelectric energy harvesting circuit for wireless remote power supply *IEEE Trans. Power Electronics* **17** 669–76
[52] Guyomar D *et al* 2005 Toward energy harvesting using active materials and conversion improvement by nonlinear processing *IEEE Trans. Ultrasonics, Ferroelectrics and Frequency Control* **52** 584–95
[53] Shu Y and Lien I 2006 Analysis of power output for piezoelectric energy harvesting systems *Smart Mater. Struct.* **15** 1499
[54] Shu Y, Lien I and Wu W 2007 An improved analysis of the SSHI interface in piezoelectric energy harvesting *Smart Mater. Struct.* **16** 2253
[55] Lallart M and Guyomar D 2008 An optimized self-powered switching circuit for non-linear energy harvesting with low voltage output *Smart Mater. Struct.* **17** 035030
[56] Kong N *et al* 2010 Resistive impedance matching circuit for piezoelectric energy harvesting *J. Intell. Mater. Syst. and Struct.* **21** 1293–302
[57] Szarka G D, Stark B H and Burrow S G 2012 Review of power conditioning for kinetic energy harvesting systems *IEEE Trans. Power Electronics* **27** 803–15